



CHALMERS
UNIVERSITY OF TECHNOLOGY

Formation of Soot in Oxygen-Enriched Turbulent Propane Flames at the Technical Scale

Downloaded from: <https://research.chalmers.se>, 2024-03-13 08:43 UTC


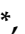

Citation for the original published paper (version of record):

Edland, R., Allguren, T., Normann, F. et al (2020). Formation of Soot in Oxygen-Enriched Turbulent Propane Flames at the Technical Scale. *Energies*, 13(1). <http://dx.doi.org/10.3390/en13010191>

N.B. When citing this work, cite the original published paper.

Article

Formation of Soot in Oxygen-Enriched Turbulent Propane Flames at the Technical Scale

Rikard Edland , Thomas Allguren , Fredrik Normann and Klas Andersson 

Department of Space Earth and Environment, Division of Energy Technology, Chalmers University of Technology, 41296 Gothenburg, Sweden; normann@chalmers.se (F.N.); klon@chalmers.se (K.A.)

* Correspondence: rikard.edland@chalmers.se (R.E.); thomas.allguren@chalmers.se (T.A.)

Received: 8 November 2019; Accepted: 24 December 2019; Published: 1 January 2020



Abstract: Soot is an important component for heat transfer in combustion processes. However, it is also a harmful pollutant for humans, and strict emissions legislation motivates research on how to control soot formation and release. The formation of soot is known to be triggered by high temperature and high pressure during combustion, and it is also strongly influenced by the local stoichiometry. The current study investigates how the formation of soot is affected by increasing the oxygen concentration in the oxidizer, since this affects both the temperature profile and partial pressures of reactants. The oxygen-to-fuel ratio is kept constant, i.e., the total flow rate of the oxidizer decreases with increasing oxygen concentration. Propane is combusted ($80 \text{ kW}_{\text{th}}$) while applying oxygen-enriched air, and in-flame measurements of the temperature and gas concentrations are performed and combined with available soot measurements. The results show that increasing the oxygen concentration in the oxidizer from 21% to 27% slightly increases soot formation, due to higher temperatures or the lower momentum of the oxidizer. At 30% oxygen, however, soot formation increases by orders of magnitude. Detailed reaction modeling is performed and the increase in soot formation is captured by the model. Both the soot inception rates and surface growth rates are significantly increased by the changes in combustion conditions, with the increase in soot inception being the most important. Under atmospheric conditions, there is a distinct threshold for soot formation at around $1200 \text{ }^{\circ}\text{C}$ for equivalence ratios >3 . The increase in temperature, and the slower mixing that results from the lower momentum of the oxidizer, have the potential to push the combustion conditions over this threshold when the oxygen concentration is increased.

Keywords: combustion; flame; soot; oxygen-enrichment; propane

1. Introduction

Emissions of soot from combustion processes in engines, boilers, and other industrial processes can have hazardous effects on human health and are detrimental for the environment [1–4]. The allowed limits of particulate (PM) matter emission in the industrialized world have become stricter over the past decades, and even more stringent legislation is expected in the near future. An illustration of upcoming legislation is the European Union (EU) Directive 2016/2284/EU [5], which, e.g., states that the EU should reduce its emissions of $\text{PM}_{2.5}$ by 20% (compared to 2005 levels) in the time period of 2020–2029, and by 49% for any year after 2030. Although secondary measures exist for mitigation of soot and larger PM, such as filters and electrostatic precipitators, it is often expensive or impractical to install such measures, depending on the specific application. Furthermore, the presence of soot can be beneficial, as it increases heat radiation and can promote more efficient heat transfer. Therefore, understanding and controlling soot formation in combustion systems are topics of great interest. Apart from burners and engines, the formation of carbonaceous nanoparticles is also important for material sciences, e.g., the use of nanotubes [6–8].

The formation of soot is a complex process that comprises several steps. These steps are described in detail in reviews of soot formation [9–12], so only a brief overview is provided here. The first step is fuel pyrolysis and the production of radicals and intermediate gas species. Some of the species produced during fuel pyrolysis may, depending on the reaction conditions, react further and form larger compounds, e.g., polycyclic aromatic hydrocarbons (PAH), which are crucial for soot formation. The species emerging from fuel pyrolysis are strongly dependent upon the fuel used, as fuels that contain aromatic components (e.g., diesel) are more prone to form PAHs than aliphatic fuels, such as methane and propane. The second step is the formation of the initial soot particles, often referred to as ‘soot inception’ or ‘nucleation’, which encompasses the transition from the gas phase to the particulate phase. This step is not fully understood, since there is no defined demarcation between soot precursors and soot particles. In physical terms, mature soot particles typically have diameters >10 nm, while nascent particles are often assumed to have diameters in the range of 1–5 nm [13,14]. Previous studies have indicated that these early particles are liquid-like and easily flattened [15], and they are thus sometimes referred to as nanoparticles or nano-organic carbon rather than soot particles [16]. Chemically, soot particles and soot precursors consist mainly of carbon and some hydrogen. Nascent particles may have hydrogen-to-carbon (H/C) ratios of ≥ 0.5 , although as the soot matures it undergoes dehydrogenation, such that the H/C ratio of mature particles is typically ≤ 0.125 [17]. The last step in the formation of soot is growth, which occurs either through surface addition of gas-phase molecules (e.g., C_2H_2 , C_6H_6 or PAH) or by coagulation with other soot particles. Surface addition adds mass to the particles, although the number of particles remains constant, whereas coagulation keeps the total mass constant but decreases the number of particles. Particles may coalesce into larger spherical particles or agglomerate to form soot aggregates. Soot aggregates are typically chain-like clusters of soot particles of >100 nm in length.

Oxidation of soot particles and soot precursors occurs concomitantly with these steps and is, thus, a competing mechanism. The availability of oxygen in soot-forming regions is an interesting parameter as it is inherently related to temperature, which is a key parameter in determining the reaction rates. If oxygen participates rapidly in exothermic reactions with species that are not essential for soot formation, the temperatures may increase significantly while the oxygen levels remain low, thereby favoring soot formation rates over oxidation rates. The formation of soot is, therefore, significantly affected by the mixing of the oxidizer and fuel, as well as the partial pressure of oxygen in the oxidizer, which is especially interesting for combustion systems that use oxygen enrichment or pressurization. Oxygen enrichment, which may be used to increase the peak-flame temperature, decrease flue gas losses, or reduce equipment size, is applied in some industrial applications (e.g., glass manufacturing and aluminum recycling) and in oxy-fuel combustion for carbon capture. Several studies have investigated oxygen-enriched combustion for co-flowing diffusion flames experimentally [18–33], and many have noted a significant increase in soot formation when the oxygen content in the oxidizer was increased (due to higher temperatures and reaction rates). As for the impact of pressure on soot formation in laminar flames, the soot volume fraction appears to scale in proportion to the total pressure in terms of a power-law, i.e., $\propto P^n$. The value of n is often reported to lie between 1.0 and 1.5 at pressures below approximately 20 atm, depending on the fuel and combustion system used, and it decreases slightly with increasing pressure [34]. Some studies have noticed a sudden increase in soot formation (sudden change in flame color from blue to yellow) when increasing from atmospheric pressure to slightly higher pressures [35,36].

Most work on oxygen-enhanced and pressurized diffusion flames have been conducted at small scale (<1 kW_{th}) and with laminar conditions in an open space. The current work investigates the effects of oxygen-enrichment on soot formation in larger-scale (80 kW_{th}) confined turbulent diffusion flames, to assess relevance to industrial processes. The experimental results are discussed and supported with detailed reaction modeling based on our present understanding of soot formation processes.

2. Methodology

The work in this paper is based on experiments conducted in the 100-kW_{th} oxy-fuel unit at Chalmers University of Technology, Gothenburg, Sweden (Figure 1). The unit has a top-mounted burner and can apply standard air combustion, oxygen-enhanced air combustion, as well as oxy-fuel combustion of gaseous and solid fuels. The burner has a central fuel channel and two annular swirl registers. The inner swirl register has a swirl angle of 45° and a swirl number of 0.74, while the outer swirl register has an angle of 15° and a swirl number of 0.22. The swirl numbers have been calculated using the so-called ‘alternative swirl number’, which does not require information about the static pressure or velocity profiles. See, e.g., Ref [37] for more details and the equation used. Further details regarding the Chalmers unit can be found elsewhere [38,39]. In the present study, the effect of using oxygen-enriched air for propane combustion was explored. The fuel input was set to 80 kW_{th} (1.73 g/s of propane) and the stoichiometric ratio (λ) was kept constant at 1.15.

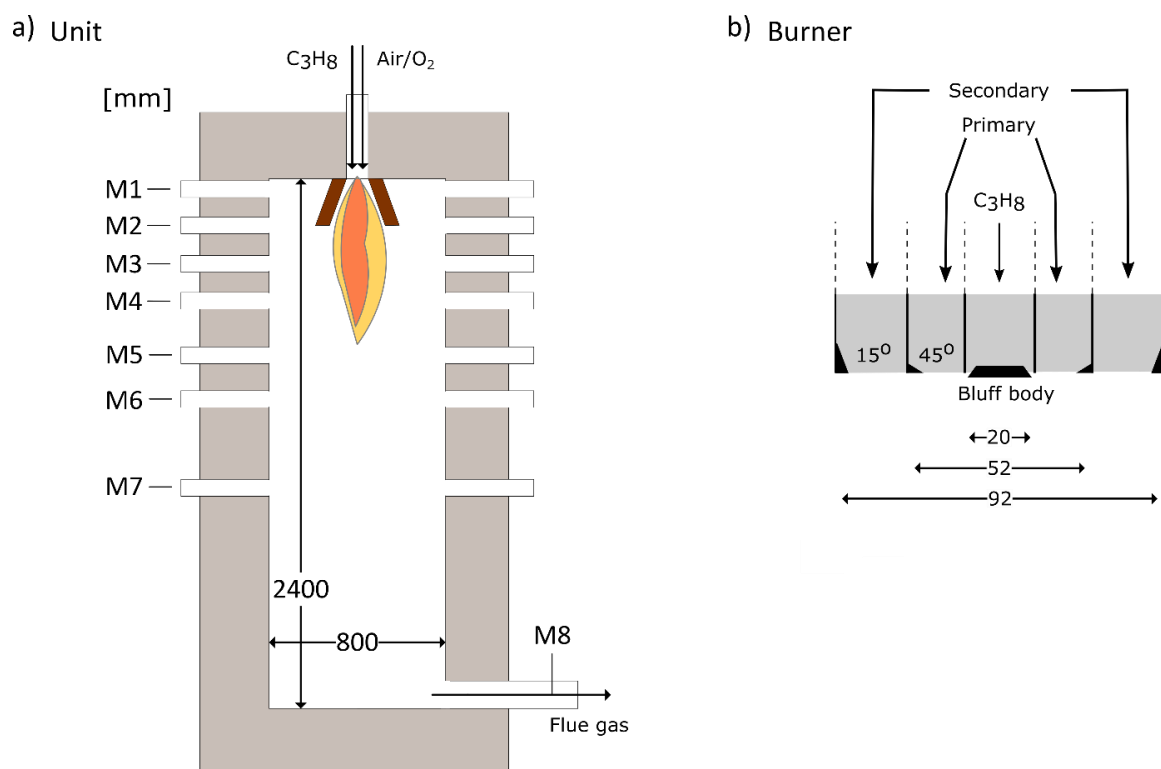


Figure 1. Schematic of the 100-kW_{th} oxy-fuel unit at Chalmers University of Technology. Illustration (a) presents dimensions and overall layout of the unit, with M1–M8 indicating measurement ports. Illustration (b) depicts the burner design with corresponding diameters and swirl angles. All distances are given in mm.

In-flame gas concentration measurements were performed with a cooled probe connected to a gas analysis system. The central pipe of the probe, through which the gases were extracted, was electrically heated so that the temperature was kept above 140 °C to avoid condensation. The probe was traversed in ports M2–M5 with seven radial positions, from the wall to the center line, in each port. The measurement ports M2–M5 were located 239, 361, 531, and 801 mm from the burner, respectively. The gas analysis system used paramagnetism (O₂), non-dispersive ultraviolet sensors (SO₂), non-dispersive infrared sensors (CO and CO₂), and chemiluminescence (NO and NO₂). In-flame measurements of temperature were performed with a suction pyrometer (thermocouple type B). Soot measurements using laser-induced incandescence (LII) and a scanning mobility particle sizer (SMPS) were available for this unit from previous work [40,41]. The LII-measurements were performed at port M3 and the SMPS measurements were performed at ports M2–M5. The LII technique is

based on heating soot particles by exposing them to laser pulses and measuring the increased light emission from the particles with a CCD (Charged Coupled Device) camera. The SMPS technique is an intrusive method where particles are extracted from the flame and the particle distribution determined based on the mobility of charged particles in electrical fields. Further details about how these measurement techniques work and how they were setup are available in the work by Simonsson et al. [42], Gunnarsson et al. [40], as well as Bäckström et al. [41]. The experimental conditions, such as fuel input and burner, were the same in these papers as in the current work.

2.1. Cases

The test matrix used for this study is shown in Table 1. All the cases were conducted using atmospheric pressure and with a global stoichiometry (λ) of 1.15. Oxidizers with an oxygen content of up to 35% were tested. In-flame gas measurements were performed for air (case Air-21) and oxygen-enriched air with 32% O₂ (Air-32). Soot measurements were, unfortunately, not available for the experiments with oxygen concentrations of 32% or 35% (Air-32 and Air-35) due to practical problems with optical access during those conditions.

Table 1. Test matrix. The number in the case-name indicates the oxygen concentration in the oxidizer. The last column refers to the availability of soot measurements from previous work.

Cases	O ₂ Injection g/s	Oxidizer Flow g/s	O ₂ in Oxidizer vol% Dry	O ₂ in Flue Gases vol% Dry	In-Flame Gas Measurements	Soot Measurements LII	Soot Measurements SMPS
Air-21	0	30.99	21	2.95	Yes	Yes	Yes
Air-25	1.45	26.18	25	3.57	No	Yes	No
Air-27	2.01	24.31	27	3.89	No	Yes	No
Air-30	2.72	21.97	30	4.37	No	Yes	No
Air-32	3.11	20.65	32	4.70	Yes	No	No
Air-35	3.62	18.96	35	5.20	No	No	No

2.2. Model

A plug flow reactor (PFR) model is used to investigate the flame chemistry under specified conditions. The PFR has two inlets: one for the fuel (C₃H₈), and one for the oxidizer. The oxidizer is introduced gradually to the PFR to simulate the availability of oxygen that the fuel experiences during mixing. The amount of added oxidizer at certain distances from the inlet point is set by the user and is referred to as the “injection profile”. The axial temperature profile is also set by the user, i.e., the temperature profile is not calculated by the model. Although this makes the model non-predictive, it is set up in this way so as to avoid errors related to estimating heat losses to the walls and to allow use of the in-flame temperature measurements as input to the model. The kinetics of combustion and soot formation are described by the detailed reaction mechanism of Richter et al. [43]. The mechanism consists of 6654 reactions, which describe conventional gas-phase reactions, the PAH chemistry, and soot particle growth and oxidation. The molecules are divided into groups that differ with respect to size, termed BIN1–BIN20, with the smallest molecules (C₂₄H₁₂) grouped in BIN1 and the largest (C₁₂₉₇₂₀₃₂H₁₆₂₂₀₁₆) in BIN20. All the BINs can be activated by H abstraction, to form BIN radicals that are more reactive than the parent BINs. The rate constants for reactions that involve large PAHs, PAH radicals, BINs, and BIN radicals are based on the rate constants for benzene and phenyl reactions and scaled according to size, given that larger molecules/particles have more active sites. The authors of the mechanism differentiate between large PAHs and soot particles after BIN4, i.e., BIN 5 is considered to be the first soot particle. The main difference between BINs 1–4 and BINs 5–20 in the model is that BINs 5–20 can agglomerate directly with each other, while BINs 1–4 must form radicals to react with other BINs. In the current work, all the BINs are considered as soot, in order to include large molecules that may form during the transition from gas-phase precursors to solid-phase particles.

The model is implemented in the Chemkin software, and all species are treated as gas components. The Chemkin solver calculates the reaction rates at each step in the PFR using the law of mass action. Thermodynamic data is used for the reversible reactions. The resulting reaction rates and mole

fractions of all species at every distance are given as output from the model. Since soot particles may agglomerate into larger soot particles, the total molar fraction of soot can decrease even though the amount of soot remains the same. For this reason, it is often preferable to express the soot level as a volume fraction (f_v). Another relevant parameter is the number density of soot particles (N_p). Conversion from the mole fraction to these units is performed with the following equations:

$$f_v = x_{\text{soot}} \frac{M_{\text{soot}}}{M_{\text{tot}}} \frac{\rho_{\text{tot}}}{\rho_{\text{soot}}} \left[\frac{cm_{\text{soot}}^3}{cm_{\text{tot}}^3} \right] \quad (1)$$

$$N_p = x_{\text{soot}} \frac{N_A \rho_{\text{tot}}}{M_{\text{tot}}} \left[\frac{\#_{\text{particles}}}{cm_{\text{tot}}^3} \right] \quad (2)$$

where x is the mole fraction, M is the molar mass, ρ is the density (1.8 g/cm³ for soot), and N_A is the Avogadro constant. The total mole fraction of soot (x_{soot}) is obtained by adding the mole fractions of all the particle sizes. The molar mass of soot (M_{soot}) is obtained from a weighted average of the molar masses of BINs 1–20, based on the current size (Bin) distribution.

2.3. Interpretation of Experimental Results

For the interpretation of the experimental results, conditions resembling those in Case Air-21 and Case Air-32 are modeled. The used temperature profiles and oxidizer injection profiles are shown in Figures 2 and 3. For Air-21, the temperature measurements are used to define the temperature profile in the model. The oxidizer injection profile is then set so that the calculated CO profile from the model fit the CO measurements for Air-21. The concentration of CO is chosen for tuning the model since CO is an important indication of the local stoichiometry in the experimental flame. This method has been applied successfully in previous studies [44,45] to describe the combustion conditions and the chemistry of nitrogen, sulfur and alkali as well as hydrocarbon oxidation. In the case of Air-32, temperature measurements were not available due to measurement issues related to large amounts of soot clogging the suction pyrometer. Due to the lack of temperature input, two simulations are performed for Air-32. The first simulation is called Air-32-NoFit and uses the same oxidizer injection profile as in Air-21, but with 32% oxygen (retaining $\lambda = 1.15$), and the same temperature profile. The second simulation is called Air-32-Fit and uses a modified oxidizer injection profile and temperature profile. The profiles for Air-32-Fit are set so that both the calculated CO and soot levels fit the CO and soot measurements. The reported temperature and injection profiles in Figures 2 and 3 for Air-32-Fit are a combination of profiles that manages to capture the measured CO and soot levels. Since there might be other combinations of temperature and injection profiles that also fit the measurements, a sensitivity analysis is performed (described in Section 2.4). To summarize, the difference between Air-21 and Air-32-NoFit is that the latter has a higher concentration of oxygen in the oxidizer (or to be more precise, less nitrogen), and the differences between Air-32-NoFit and Air-32-Fit lie in their injection and temperature profiles.

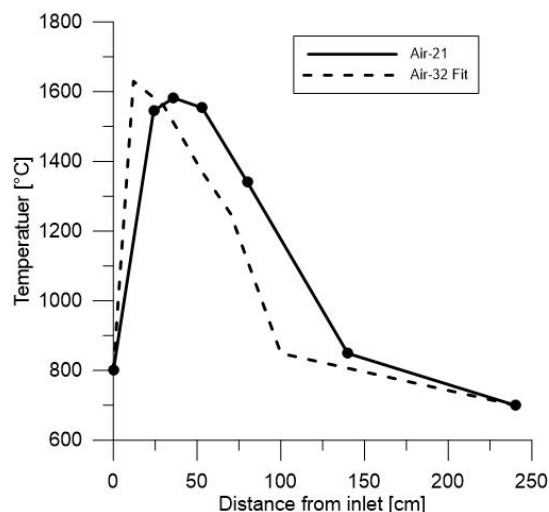


Figure 2. Temperature profiles used in the model. The temperature profile for Air-21 is based on measurements made for the Air-21 case (filled circles). The Air-32-Fit profile (dashed line) is speculative and indicates how the process could proceed. The calculated soot levels become close to the measured soot levels with this profile.

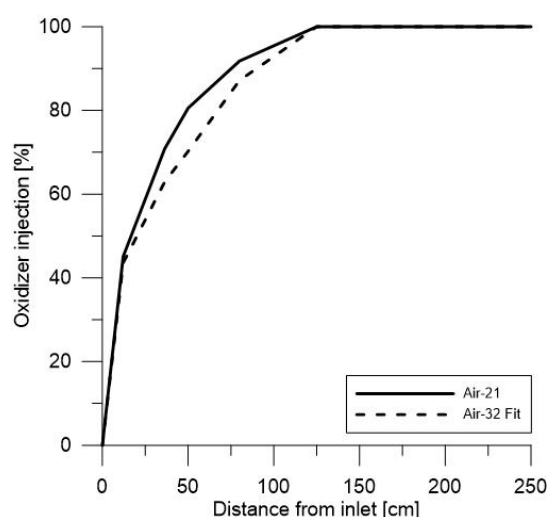


Figure 3. Oxidizer injection profile. The total amount of oxidizer injected in the Air-21 case (solid line) is 31.0 g/s and in the Air-32 Fit case (dashed line) it is 20.7 g/s.

In the investigation of combustion chemistry, the flames are divided into four distinct zones. Zone 1 stretches from the inlet of the PFR to the location with peak PAH mass concentration. This zone is crucial for soot formation, as it is here that the soot precursors are formed. Zone 2 is defined as the region between the PAH peak and the BIN1 peak. This zone represents the soot inception zone, i.e., where soot starts to form as a result of increased PAH growth. Zone 3 begins at the point where BIN1 peaks and ends where the CO levels reach zero, i.e., up to the end of the flame. The fourth (final) zone stretches to the end of the reactor and represents the post-flame zone. The rate of production (mol/cm³/s) of each species and reaction that occurs at each position in the PFR is given as output from the model. This rate can be integrated over a volume (e.g., the volume of a zone) to obtain the net production/consumption rate (mol/s) of a certain species.

2.4. Sensitivity Analysis and Φ -T Maps

A sensitivity analysis is performed to investigate the impacts on soot formation of different temperature and injection profiles. The eight profiles (four temperature profiles and four injection

profiles) shown in Figures 4 and 5 are tested individually and the results are compared to the results obtained for the Air-21 profiles. As soot formation occurs in the early sub-stoichiometric part of the flame, the focus is on the first 40 cm, and due to the already low level of soot formed in Air-21, only those conditions that promote soot formation are investigated. In the temperature analysis, profiles A–D have increased temperature gradients and temperature peaks, with profile D being the case with the steepest gradient and highest peak. In the injection profile analysis, the profiles Mix1–Mix4 have lower injection rates than the Air-21 profile, with Mix4 showing the lowest rate. The oxidizer is normal air (21% O₂) in all the runs. The isolated effect of increasing only the oxygen content (without increasing the temperature) is touched upon in the Air-32-NoFit case but is not investigated further in the sensitivity analysis.

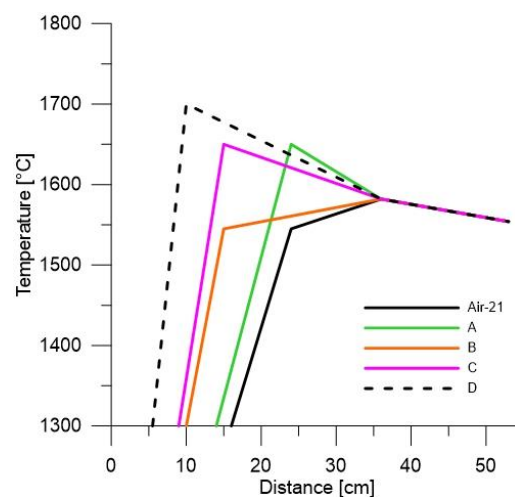


Figure 4. Temperature profiles used in the sensitivity analysis.

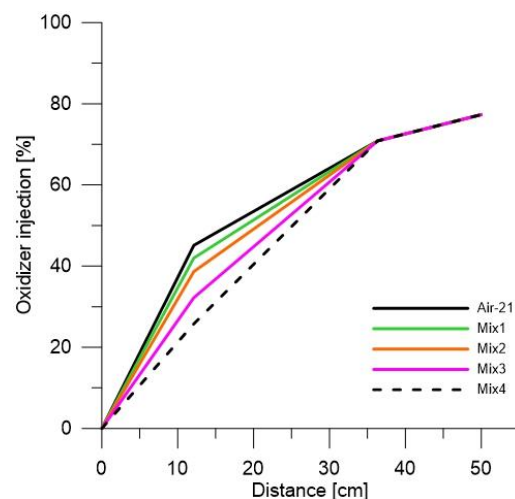


Figure 5. Oxidizer injection profiles used in the sensitivity analysis.

Fuel-to-air ratio vs. temperature maps (Φ -T maps) are created for premixed propane/air combustion, by performing simulations in isothermal perfectly stirred reactor (PSR) models with different temperatures and stoichiometries. Note that Φ represents the fuel-to-air equivalence ratio, i.e., the inverse of the λ term commonly used for burners. Φ -T maps are commonly used in diesel-related research and summarize the effects of temperature and stoichiometry on the formation of soot or other compounds. The maps used in the present work are created for fuel-to-air equivalence ratios of 0.1, 1.0, 2.0, 3.0, 4.0, 5.0, and 6.0, and for temperatures in the range of 800–2200 °C with 50 °C increments. The PSR is 1 dm³ and the propane flow is 1 g/s (residence time varied between 90 ms and 330 ms).

depending on temperature). The outlet mass flow of a component is divided by the volume of the reactor to calculate the net formation rate in $\text{mg}/\text{cm}^3/\text{s}$. The effect of pressure (1, 2, and 5 bar) is also investigated using Φ -T maps.

3. Results & Discussion

This section is divided into the following three sections: the experimental results; simulations that involve applying the model to two experimental cases (Air-21 and Air-32) and the sensitivity analysis.

3.1. Experimental Results

The in-flame measurements of O_2 and CO for Air-21 and Air-32 are shown in Figures 6 and 7 by means of filled contour maps, mirrored at the centerline. Both the O_2 and CO measurements indicate that Air-32 forms a broader flame and a generally less-oxidizing environment. High concentrations of O_2 in Air-32 are only observed close to the inlet of the oxidizer. Regarding Figure 7, the CO levels in Air-32 are 2–3-fold higher along the centerline and 5–100-fold higher at 100 mm from the centerline, as compared to Air-21. One factor that contributes to the higher CO levels is the lower level of nitrogen present in Air-32, which naturally leads to slightly larger fractions of all the species. However, two more important secondary effects of the decreased amount of nitrogen in the oxidizer need to be considered. First, the resulting increases in reaction rates (caused by the larger fractions of reactants) likely increases the early temperatures and CO production rates and, thereby, the CO concentration. Second, the momentum of the oxidizer jet is decreased, and in Air-32 the jet may not penetrate the flame as well as in Air-21, leading to slower conversion of CO. The lower momentum also explains the broader flame in Air-32. Both a high early temperature and a less-oxidizing environment promote soot formation.

Unfortunately, temperature measurements in the earliest part of the flame are not available to confirm that the temperature is higher early on, since measurement inside the quarl is not possible. Furthermore, the temperature measurements in Air-32 were problematic due to the suction pyrometer becoming clogged with soot particles, which creates uncertainty regarding the measured temperatures. Figure 8 compares the temperature measurements performed at port M3 for Air-21 and Air-32, and although the values for Air-32 are uncertain, the increase in the temperature gradient occurs further from the centerline than in Air-21, which is consistent with the broader flames observed in Figures 6 and 7.

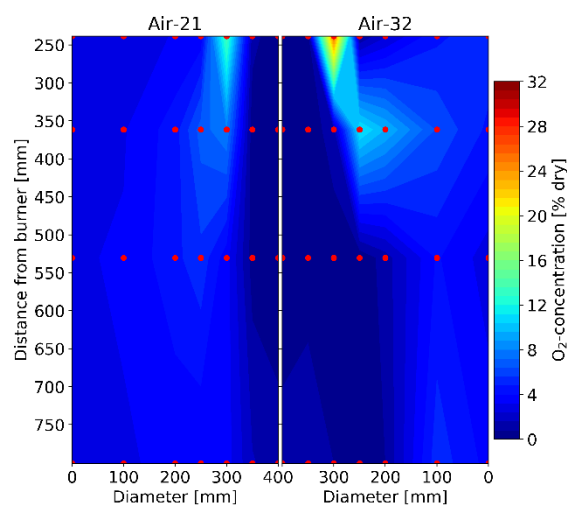


Figure 6. In-flame measurements of O_2 . The Air-21 and Air-32 cases are mirrored at the centerline. The red dots indicate measurement points performed in the four measurement ports M2–M5.

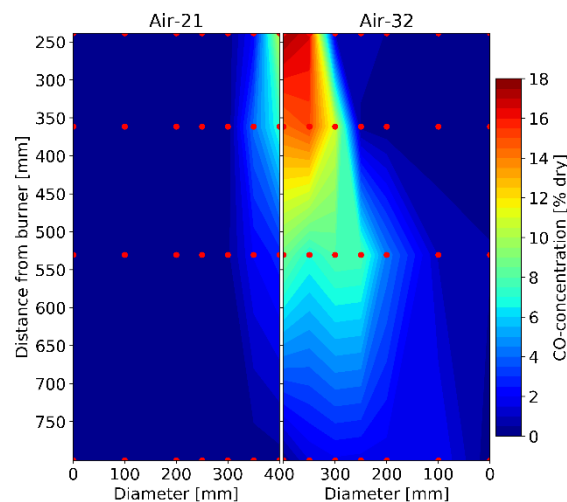


Figure 7. In-flame measurements of CO. The Air-21 and Air-32 cases are mirrored at the centerline. The red dots indicate measurement points performed in the four measurement ports M2-M5.

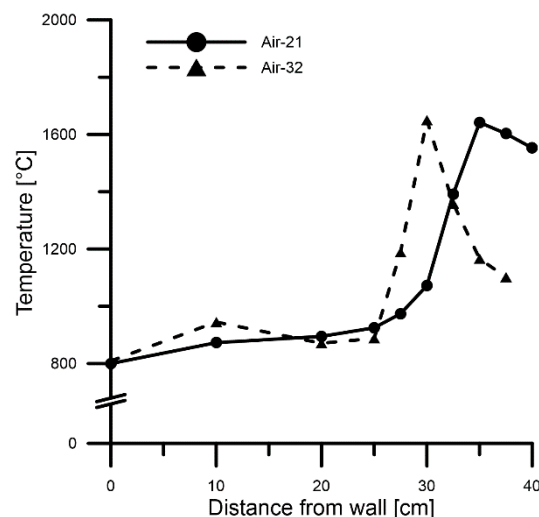


Figure 8. In-flame temperature measurements conducted at port M3 (36 cm from the burner) for the Air-21 and Air-32 cases.

Figure 9 presents images of the flames for the Air-21 and Air-30 cases acquired at port M3. While LII-measurements were not available for Air-32, there was no visual difference in the flame between Air-30 and Air-32, and the soot levels are assumed to be similar. The photographs in the top panels of Figure 9 were taken with a conventional camera using an exposure time of 1 ms. Air-30 creates a significantly more luminous flame than Air-21, and the soot radiation fills up the entire field of view, whereas in Air-21 large areas of the image are black. Visually, the human eye experiences the flame in Air-21 as mostly blue. However, to capture this, the exposure time needs to be longer, leading to a blurrier image. The bottom panels in Figure 9 show the LII images taken with a CCD camera (which captures the incoming LII-signal from the particles in the laser sheet). The local peak soot volume fraction (in M3) measured in Air-21 was around 30 ppbv, while that measured in Air-30 was around 6000 ppbv. Similar to the photos obtained using the conventional camera, the LII images show that the soot is more spread out in Air-30. The images taken with the conventional camera and the CCD camera were not taken at the same time.

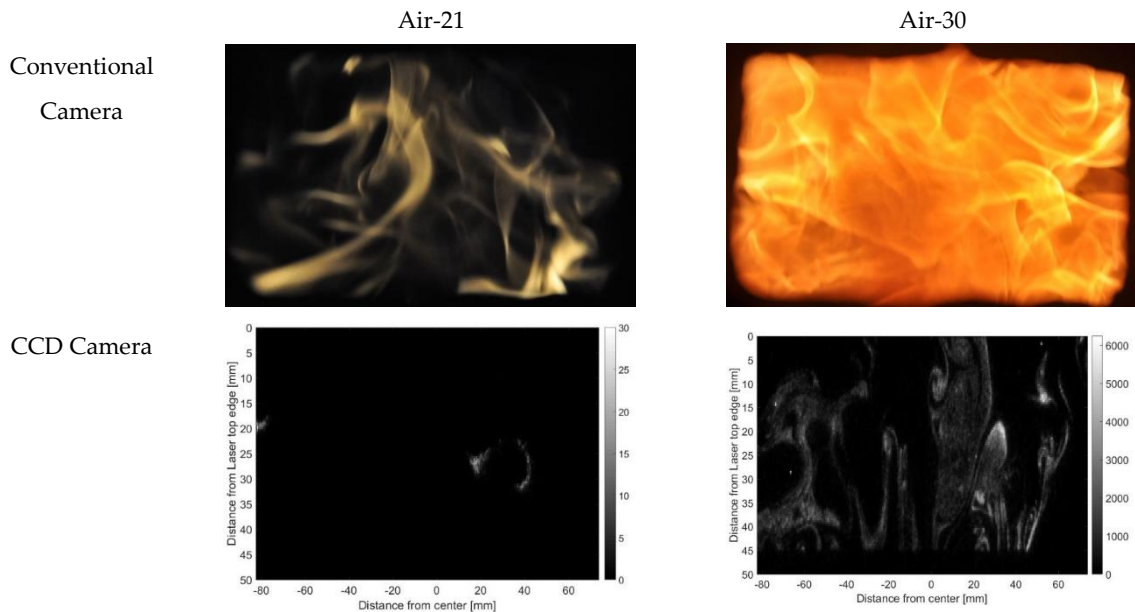


Figure 9. Photographs of the flames in the Air-21 and Air-30 cases, taken with an exposure time of 1 ms. The CCD camera captures the incoming LII-signal from the soot particles in the laser sheet.

The impact of oxygen content in the oxidizer on soot formation, based on LII-measurements, is summarized in Figure 10 over the range of 21%–30% O_2 . The NO emission from the unit exhibited an interesting behavior and is included as an easily measured component that provides information about the flame chemistry, even though it was only measured at the outlet. As the oxygen content increased up to 27%, the soot levels remained low and the NO levels increased. However, between oxygen contents of 27% and 30%, the soot formation increased by orders of magnitudes and the levels of NO_x emission decreased drastically. A similar shift in soot level has previously been observed in the same unit when applying oxy-fuel combustion (a mixture of O_2 and CO_2 as oxidizer, instead of O_2 and N_2), albeit with around 40% O_2 in the oxidizer [46]. That higher O_2 levels (40% instead of 30%) are required for the sudden increase in soot levels in oxy-fuel combustion suggests that this is a thermal phenomenon, since CO_2 has a higher heat capacity than N_2 and achieves a lower temperature for the same specific heat duty. It is worth mentioning that the LII measurements were only performed in port M3 and that the soot concentration peak is likely to be located at different distances from the burner in each case. It is thus possible that the soot measurements occur at different relative locations in the different flames. However, the drastic increase in measured soot concentration after the O_2 content reach 30% indicates a complete change in flame type, which is also indicated by the sudden decrease in outlet NO concentration. The increase in outlet level of NO with increasing O_2 content in the oxidizer up to 27% is expected, since both the temperature and partial pressure oxygen will increase and facilitate thermal NO formation. The reason for the sudden decrease in outlet NO between 27% and 30% O_2 is less clear. Possible explanations for this include cooling of the flame through heat radiation as a consequence of the increased amount of soot, increased heterogeneous reduction of NO by soot, or a fundamental change in flame chemistry and radical pool composition. As mentioned in Section 1, similar effects have been observed by other authors [33,47]. Although the nitrogen chemistry is interesting in its own right, it requires significant attention and deserves its own investigation, and the present study thus focuses on soot formation.

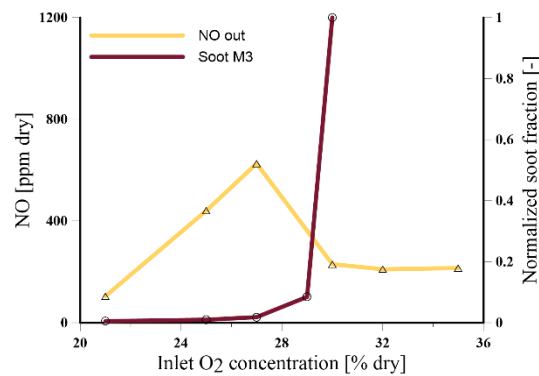


Figure 10. Measured outlet NO concentrations and normalized soot volume fractions at port M3 as a function of the oxygen content in the oxidizer.

The time-log of one particular test run of Air-30 is presented in Figure 11, where the shift to a sooty flame is signaled by the drop in outlet NO concentration. The shift to a sooty flame did not occur immediately after shifting to the higher inlet concentration of oxygen at time 0. Instead, it occurred after stable operation at Air-30 for around 20 minutes. This supports the notion that the shift is a thermal effect, as the quarl at the burner inlet may not have been sufficiently warm initially to “activate” the shift to a sooty flame. The small increase in outlet O_2 concentration (about 0.5 vol.%), which is likely due to the incomplete oxidation of soot, should also be noted.

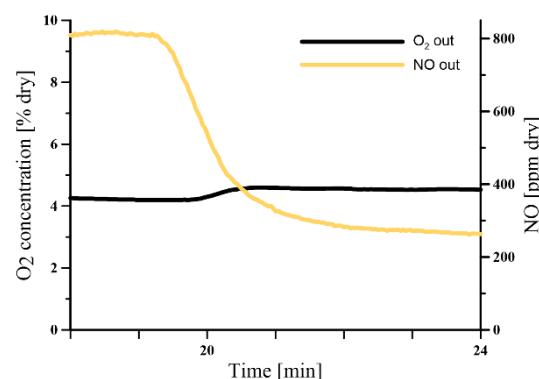


Figure 11. Outlet NO and O_2 concentrations as a function of time during stabilization of Air-30.

3.2. Interpretation of Results for Air-21 and Air-32 Cases

Figures 12–14 present the calculated values from the model for CO, O_2 , and soot for the Air-21, Air-32-NoFit, and Air-32-Fit cases, as compared with the corresponding measured values. There is a good fit between the modeled and in-flame measurements of CO and O_2 , which is expected since these measurements were used to determine the injection profiles. Since Air-32-Fit used the soot measurement as input to derive the temperature and injection profiles, a good fit is naturally achieved for soot as well (Figure 14). The fact that the model manages to capture the excessive levels of soot observed in the experiments, without inducing extreme changes in the temperature and injection profiles, is encouraging and strengthens the model. That there is good agreement between the calculated and measured soot values in the Air-21 case also indicates that the model possesses some predictability for soot formation (assuming that BINs 1–4 can be considered soot). Air-32-Fit overestimates the outlet O_2 concentration (at 240 cm) by about 0.8 vol.% compared to the measured value (Figure 13). Thus, in the model, there is a significant amount of unburnt fuel (in the form of soot) at the outlet. A possible reason for this is that the used reaction mechanism, which was developed for fuel-rich conditions and focuses on soot oxidation by O and OH, under-predicts the amount of soot that is oxidized in the oxygen-rich regions. Soot oxidation by O_2 is absent from the mechanism,

and the soot is therefore not oxidized at all in the post-flame region. If there are O_2 -rich regions in the flame as well, the model underpredicts the oxidation of soot in such regions. However, since the model captures the drastic increase in soot formation, it is nonetheless of great interest to investigate the combustion chemistry causing this occurrence. At this point, it must also be pointed out that significant levels of soot were present at the outlet in the experiments, i.e., not all soot was oxidized in the experiments either. The soot number density profiles shown in Figure 15 reveal that during the early stages of combustion, there are about three orders of magnitude more particles present for Air-32-Fit than for Air-21. The number of particles then quickly drops for Air-32-Fit, signifying rapid coagulation. For the Air-32-NoFit cases, there is about one order of magnitude more particles initially compared to the Air-21 case, and no significant particle coagulation is observed.

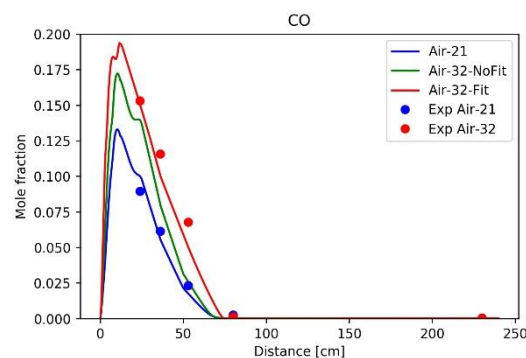


Figure 12. CO profiles calculated by the model compared with measurements conducted along the centerline.

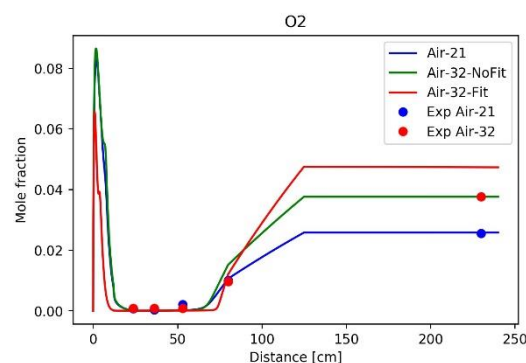


Figure 13. Calculated and measured axial O_2 concentration profiles on a wet basis.

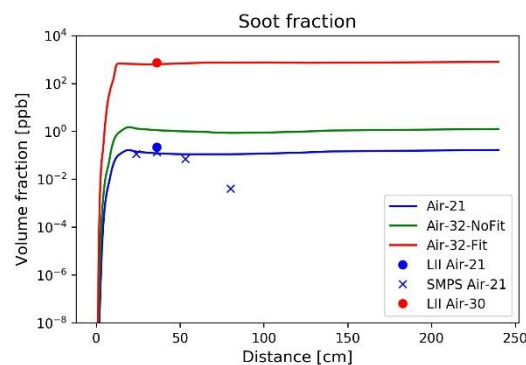


Figure 14. Soot volume fraction profiles calculated by the model compared with the LII-measurements at port M3, as well as the SMPS measurements from previous work.

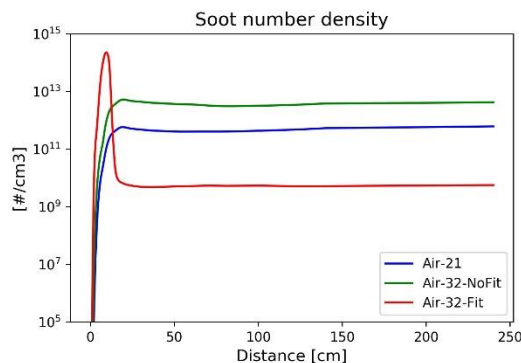


Figure 15. Calculated soot number density profiles for the three cases.

Figure 16 presents the mass flows of BINs 1–20. Comparing Air-21 and Air-32-Fit, two important differences stand out. First, in Air-21, BIN1 predominates, while in Air-32-Fit, the soot particles grow quickly to the largest size (BIN20). This is in accordance with the results obtained for the number density profiles (Figure 15). Second, the total soot mass flow is about 3000-fold higher in Air-32-Fit. There are two possible reasons for the increase in soot mass: (1) an increase in soot inception rate, or (2) an increase in the net surface growth rate. While an increase in soot inception rate will not increase the soot mass significantly on its own, it will increase the number of particles that can accumulate mass through surface growth. To investigate the importance of soot inception and surface growth, a reaction analysis is conducted for the four flame zones described in the Methodology section. Tables 2 and 3 present the net production rates of BIN1 (here considered as nascent soot) and C_2H_2 (arguably the most important species for surface growth), respectively. The net production of BIN1 in the first two zones is 200-times higher for Air-32-Fit than for Air-21. Since the total mass of soot is about 3000-fold higher, the increase in surface growth rate should be about 15-times higher in Air-32-Fit compared to Air-21. Thus, the increase in soot inception rate appears to be more important than the increase in surface growth rate. It is also interesting to note in Tables 2 and 3 that the production of BIN1 occurs concomitant with the production of C_2H_2 (both are positive in Zone 2) for Air-32-Fit, which is not the case for Air-21.

Figure 17 presents the concentration profiles of C_2H_2 , PAHs, and CO in the flame, as well as the locations of the four zones, and it is evident that Air-32-Fit differs mainly with respect to higher early concentrations of all species, as well as a more compressed Zone 2, i.e., the PAH peak and the BIN1 peak are much closer to each other in Air-32-Fit. When Zone 2 ends, i.e., when BIN1 peaks, the C_2H_2 concentration is nine times higher and the PAH concentration is 140-times higher. Therefore, an increase in surface growth rate of about 15 seems reasonable. The decrease in C_2H_2 in Zone 2 for Air-32-Fit, as shown in Figure 17, is simply the result of a dilution effect of the injected oxidizer.

The only difference in input between Air-21 and Air-32-NoFit is the lower level of nitrogen present in the oxidizer for Air-32-NoFit, which naturally leads to higher concentrations of all the other gases. This in turn increases the rates of all the reactions. In Figure 16, it appears that this increase in reaction rates increases 5–6-fold the soot mass. This is in accordance with the earlier conclusions drawn from the experimental results, i.e., that the secondary effects (increased temperatures and decreased mixing rate) are more important than the isolated effect of the decreased level of nitrogen. In Air-32-NoFit, BIN1 predominates but rapid coagulation appears to occur in the post-flame region, as low levels of mainly BIN20 are produced.

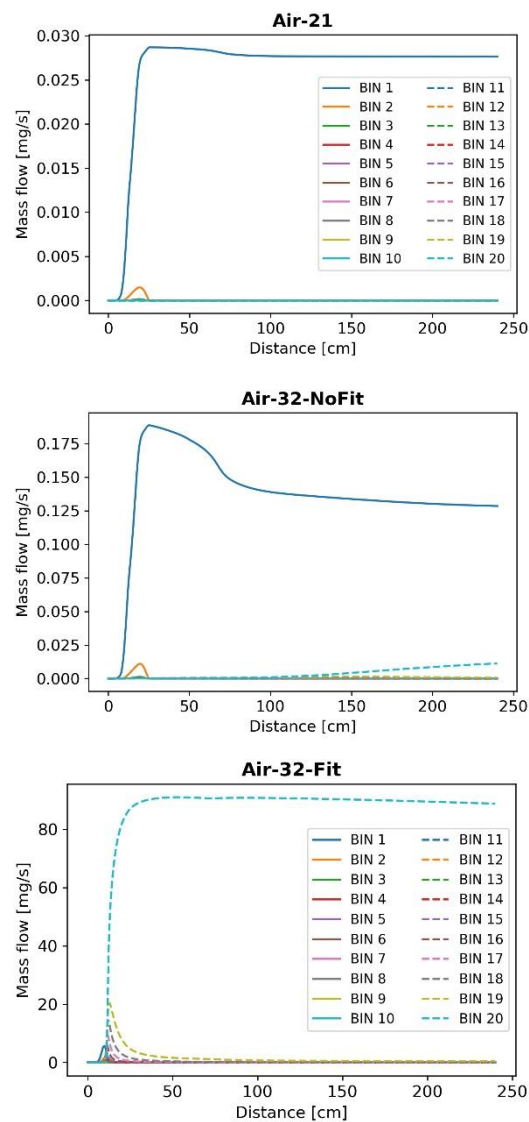


Figure 16. Mass flows of BIN1-BIN20 for the Air-21, Air-32-No Fit, and Air-32-Fit cases.

Table 2. Rates of production of BIN1 in combustion zones 1–4. Values shown are in mg/s.

Cases		Zone 1	Zone 2	Zone 3	Zone 4
BIN1	Air-21	6E-04	0.027	−0.002	0.002
	Air-32-NoFit	0.003	0.178	−0.041	−0.014
	Air-32-Fit	0.038	5.483	−5.524	0

Table 3. Rates of production of C_2H_2 in combustion zones 1–4. Values shown are in mg/s.

Cases		Zone 1	Zone 2	Zone 3	Zone 4
C_2H_2	Air-21	84.6	−38.3	−46.3	0
	Air-32-NoFit	73.61	−25.00	−48.60	0
	Air-32-Fit	154	93	−247	0

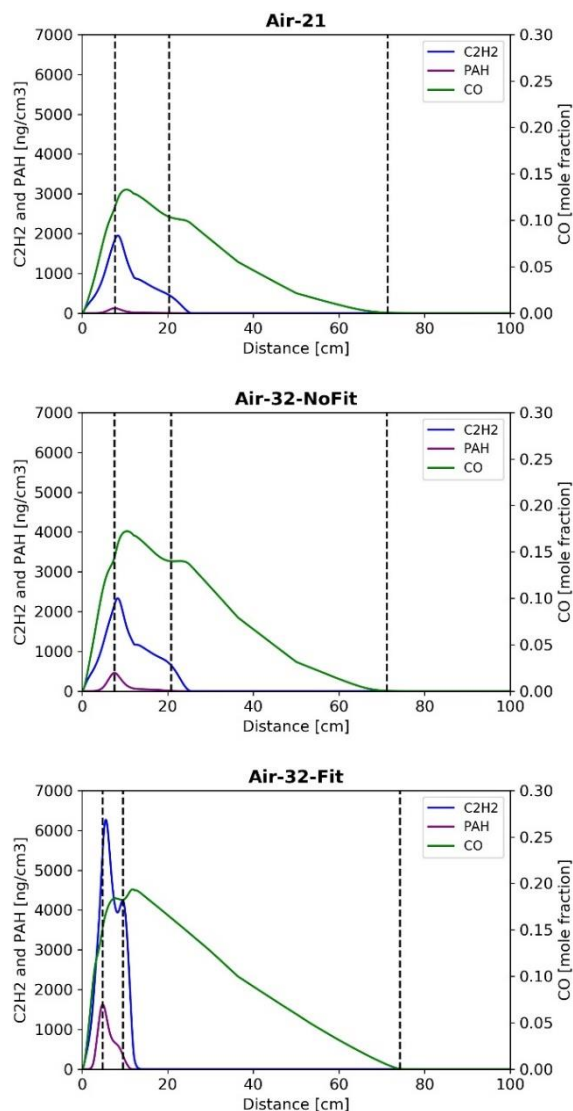


Figure 17. Profiles of the mass concentrations of C_2H_2 and PAHs and the molar fraction of CO.

From the analysis so far, the main reason for the drastically increased soot formation appears to be that soot inception is significantly enhanced in Air-32. We have defined soot inception as the production of BIN1, which in the mechanism, is formed from 600 different reactions involving PAH, PAH radicals, and smaller hydrocarbons. According to the simulations, the main reactions leading to the formation of BIN1 involve one large PAH (mainly acenaphthylene or some form of pyrene) radical reacting with a smaller hydrocarbon (usually C_6H_6 or C_2H_2). All these species are available at significantly higher concentrations in Air-32-Fit than in Air-21 and Air-32-NoFit. It is however not a trivial task to implicate any one reaction pathway in the sudden increase in soot formation. A qualitative analysis can, however, be made with the use of Φ -T maps. Figure 18 shows the Φ -T map for propane/air, as calculated by the mechanism, with lines representing Air-21 and Air-32. The lines are plotted according to the amount of oxygen that has been injected at each step of the PFR, as well as the current temperature at that step. The map shows regions in which the net formation of benzene (an important precursor), BIN1 (the first soot species), and the sum of BINs 1–20 (total soot) predominate in terms of propane combustion according to the model. The Φ -T maps themselves do not show the progress of the combustion, since every point on the map represents the net formation rate under constant, premixed conditions (i.e., temperature and gas composition). In a diffusion flame, as well as in the PFR simulations, the conditions change rapidly and the residence time at each step varies.

Although care should be taken when comparing premixed combustion systems with diffusion flames, it is clear that the temperature-stoichiometry conditions in Air-32 are more beneficial for soot formation. The Φ -T map reveals a steep gradient of soot formation at about 1200 °C for equivalence ratios >3, which corresponds well to the step-like change in soot formation observed in the experiments when an oxygen content of 30% was reached.

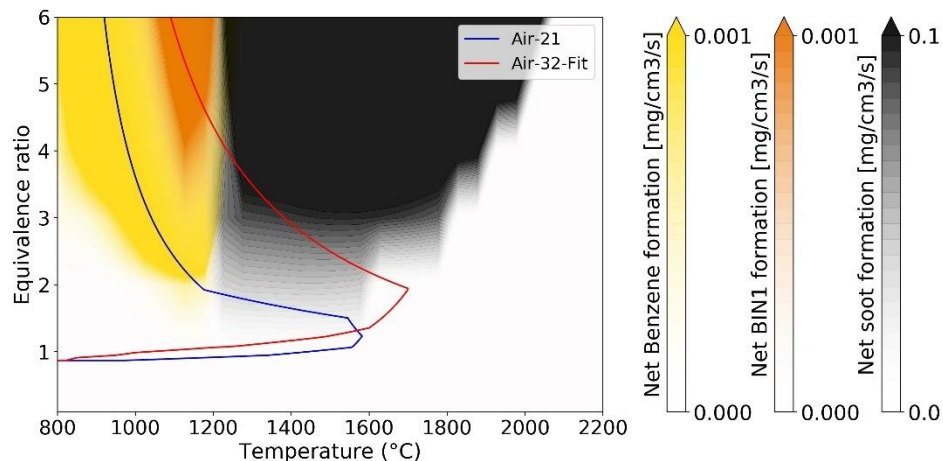


Figure 18. Φ -T map for propane with air, displaying the filled contours for benzene, BIN1, and soot formation. The colors are capped at 0.001 mg/cm³/s for benzene and BIN1 and at 0.1 mg/cm³/s for soot, i.e., values that are higher than these have the same color.

It is clear from both the experiments and the modeling that the flames formed in Air-21 and Air-32 differ significantly not only in soot formation but also in flame chemistry. Figures 19 and 20 present the concentration profiles of H and OH in the simulations since these are fundamental to the flame characteristic. Both H and OH concentrations rise earlier in Air-32 which is reasonable due to the higher early temperatures. However, since the soot formation process also advances more rapidly in Air-32, the concentrations of H and OH radicals are not very different between the cases when related to the soot formation progress. It is however interesting to note that OH levels are significantly lower in the main part of the flame. This can potentially be an important part in explaining the decrease in NO formation observed in the experiments.

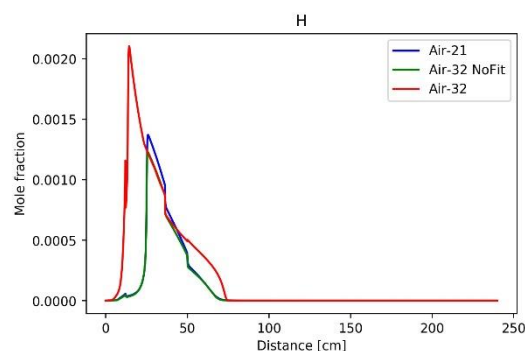


Figure 19. Concentration profiles of the H radical for the three cases.

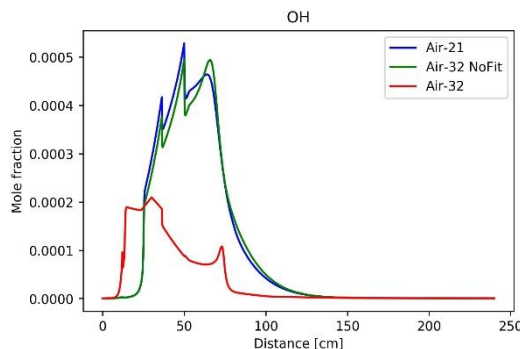


Figure 20. Concentration profile of the OH radical for the three cases.

3.3. Sensitivity Analysis

This section is divided into two parts. First, the impacts of altering the temperature and injection profiles are evaluated and discussed. Then, the connection between oxygen-enrichment and total pressure is assessed.

3.3.1. Temperature and Injection Profiles

Panels a–d in Figure 21 present the soot volume fraction profiles and the soot number density profiles resulting from the sensitivity analysis. From the temperature analysis, it can be concluded that soot formation is more sensitive to the temperature gradient than to the peak temperature. This is clear from comparing the results from Air-21 and profiles A and B. Profile A has the highest peak temperature (see Figure 4) and results in slightly higher soot formation than Air-21, while Profile B has the same peak temperature as Air-21 but has a steeper temperature gradient, which results in significantly higher soot formation. Profiles B and C show almost identical temperature gradients, although profile C reaches a higher peak temperature. However, this does not result in higher soot formation. When temperature profile D is used, soot formation is increased by about two orders of magnitude and thus appears to have crossed a soot-forming threshold. From the mixing analysis, it can be seen that lower mixing gradients increase soot formation. With injection profile Mix4, the rate of soot formation reaches levels similar to those seen when temperature profile D is used in the temperature analysis.

In both profile D and Mix4, the soot number density is reduced and, thus, indicates significant particle coagulation. When injection profile Mix3 is used, the number density profile decreases more slowly than it does for Mix4, indicating a slower and more continuous particle coagulation process. Panels e–f in Figure 21 show the sensitivity runs plotted against the Φ -T maps for propane. As expected, the run using profile D and the run using Mix4 are closer to the sooting region than the other lines. According to the maps, profile D looks like it is going through more of the sooting region than Mix4, although the amount of soot is almost the same when one considers the soot volume fraction. This is likely an effect of the difference in residence time between the soot-formation regions. For the high-temperature case (profile D), the residence time in the soot-forming regions is relatively short due to the gas expansion.

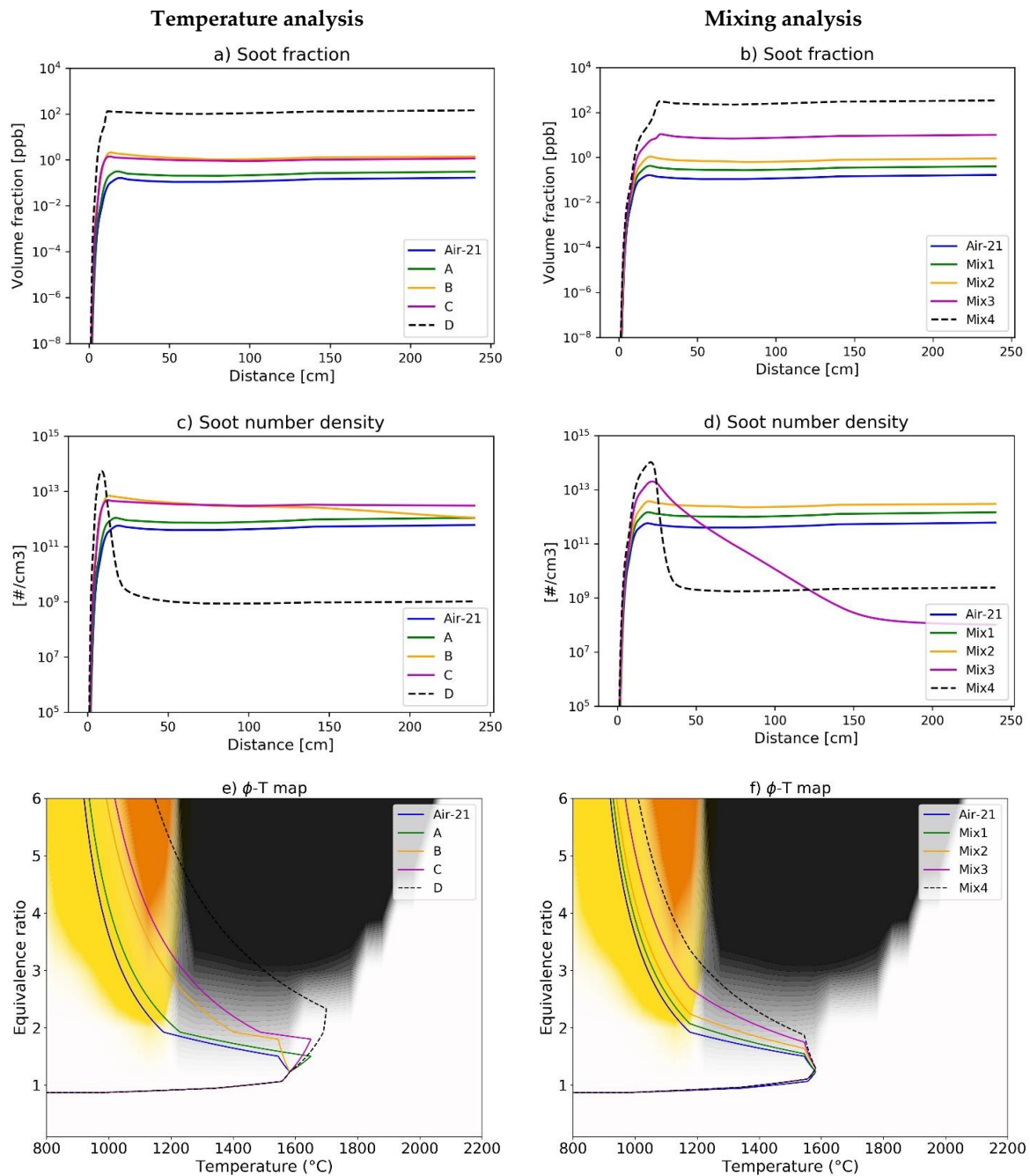


Figure 21. Soot profiles for the sensitivity cases. (a) soot volume fraction profiles for cases where the temperature profile is changed; (b) soot volume fraction profiles for cases where the injection profile is changed; (c) soot number density profiles for cases where the temperature profile is changed; (d) soot number density profiles for cases where the injection profile is changed; (e,f) the combustion processes plotted in Φ -T maps for the sensitivity cases. Yellow shading indicates benzene, orange shading indicates BIN1, and black shading indicates total soot. See Figure 18 for scales.

3.3.2. Pressure Dependence

There is a strong connection between increasing oxygen content (while keeping λ constant) and increasing total pressure, since both lead to an increase in the partial pressures of the oxygen and fuel. Figure 22 shows the soot-forming threshold of $0.1 \text{ mg/cm}^3/\text{s}$ for three Φ -T maps created using pressures of 1, 2, and 5 bar for propane/air (black lines), as well as one map with pressure of 1 bar and 42% oxygen (purple line). Focusing on the pressure, it is clear that the sooting region expands

to lower temperatures when the pressure is increased from 1 bar to 5 bar, with the biggest difference seen between 1 bar and 2 bar. This agrees well with the results of Bento et al. [36], who observed a steep increase in soot formation for laminar propane diffusion flames when going from 0.1 MPa to 0.2 MPa, which they at the time did not explain. Increasing the total pressure to 2 bar is the equivalent of increasing the oxygen content from 21% to 42% (if λ is kept constant), and although the soot-forming region (purple line in Figure 22) stretches down to less fuel-rich stoichiometries than the case with 2 bar, the lower temperature limit has moved to the same temperature (around 1200 °C). This confirms that similar effects can be expected when one increases the pressure as when one increases the oxygen content. However, the effects are not identical, since pressure and oxygen-enrichment have different effects on flame shape and residence times.

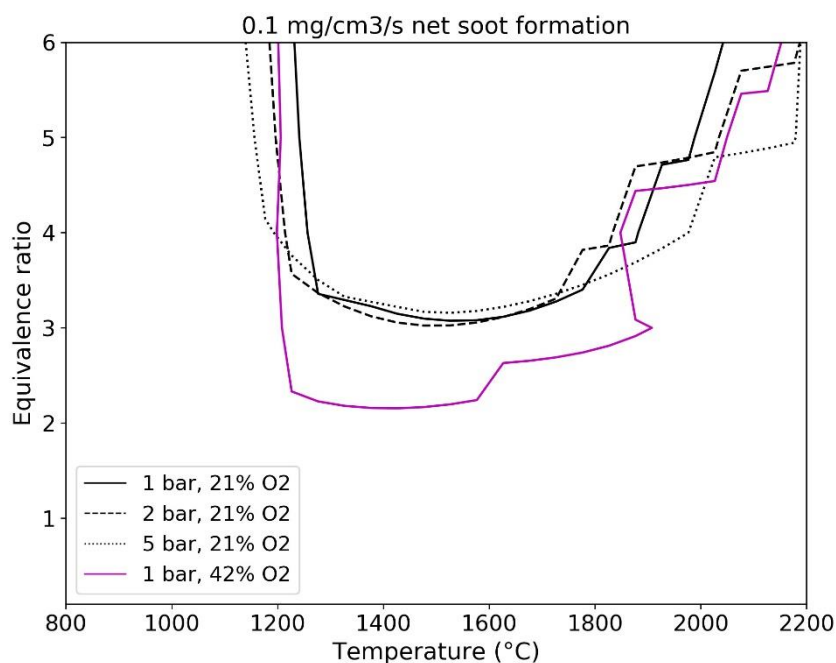


Figure 22. Contour plots for different pressures used. The lines indicate the threshold for a net soot formation of 0.1 mg/cm³/s.

4. Conclusions

Experiments with oxygen-enriched air applied to an 80-kW confined swirled propane flame were performed to investigate the effects on combustion conditions and soot formation. In-flame temperature and gas composition measurements were performed and combined with available soot concentration measurements to characterize the flame. The experiments reveal that soot formation expresses a threshold dependence for the inlet oxygen concentration (and the conditions related to the inlet oxygen concentration). The response in terms of soot formation to increased oxygen concentration is weak until the O₂ concentration in N₂ is around 30%, at which point a dramatic increase in soot formation occurs.

The drastic increase in soot formation is also seen in a state-of-the-art reaction mechanism for soot formation applied to the relevant conditions. The relationship between temperature and local stoichiometry (i.e., mixing), both of which are conditions affected by the inlet O₂ concentration, controls the point of the soot-formation threshold. The modeling indicates that the triggers for the increase in soot formation are (primarily) an increased soot inception rate and (secondarily) increased surface growth rates. Although the modeling confirms the observed effect on soot formation by changes in combustion settings, the underlying mechanism is not fully understood. For future work, further investigations of PAH chemistry and interactions with, for example, the radical pool, are recommended.

Author Contributions: Conceptualization, F.N. and K.A.; Funding acquisition, K.A.; Investigation, R.E. and T.A.; Methodology, R.E. and T.A.; Project administration, K.A.; Supervision, T.A., F.N. and K.A.; Visualization, R.E.; Writing—original draft, R.E.; Writing—review & editing, T.A., F.N. and K.A. All authors have read and agreed to the published version of the manuscript.

Funding: This research was funded by the Swedish Energy Agency and LKAB, grant number P37204-1. The APC was also funded by P37204-1.

Acknowledgments: The Swedish Energy Agency and LKAB are acknowledged for the financial support of this work. Adrian Gunnarsson is acknowledged for his help during measurements and Johan Simonsson for providing LII-data.

Conflicts of Interest: The authors declare no conflict of interest.

References

1. Dockery, D.W.; Pope, C.A.; Xu, X.; Spengler, J.D.; Ware, J.H.; Fay, M.E.; Ferris, B.G., Jr.; Speizer, F.E. An association between air pollution and mortality in six US cities. *N. Engl. J. Med.* **1993**, *329*, 1753–1759. [[CrossRef](#)] [[PubMed](#)]
2. World Health Organization. *WHO Air Quality Guidelines for Particulate Matter, Ozone, Nitrogen Dioxide and Sulphur Dioxide*; Global Update 2005; Summary of Risk Assessment; World Health Organization: Geneva Switzerland, 2005.
3. Brunekreef, B.; Holgate, S.T. Air pollution and health. *Lancet* **2002**, *360*, 1233–1242. [[CrossRef](#)]
4. Highwood, E.J.; Kinnerson, R.P. When smoke gets in our eyes: The multiple impacts of atmospheric black carbon on climate, air quality and health. *Environ. Int.* **2006**, *32*, 560–566. [[CrossRef](#)] [[PubMed](#)]
5. Parliament, E. Directive (EU) 2016/2284 of the European Parliament and of the Council of 14 December 2016 on the reduction of national emissions of certain atmospheric pollutants, amending Directive 2003/35/EC and repealing Directive 2001/81/EC (Text with EEA relevance). *OJL* **2016**, *344*, 1–31.
6. Merchan-Merchan, W.; Saveliev, A.V.; Kennedy, L.; Jimenez, W.C. Combustion synthesis of carbon nanotubes and related nanostructures. *Progress Energy Combust. Sci.* **2010**, *36*, 696–727. [[CrossRef](#)]
7. Richter, H.; Treska, M.; Howard, J.B.; Wen, J.Z.; Thomasson, S.B.; Reading, A.A.; Jardim, P.M.; Vander Sande, J.B. Large scale combustion synthesis of single-walled carbon nanotubes and their characterization. *J. Nanosci. Nanotechnol.* **2008**, *8*, 6065–6074. [[CrossRef](#)]
8. Unrau, C.J.; Axelbaum, R.L.; Fraundorf, P. Single-walled carbon nanotube formation on iron oxide catalysts in diffusion flames. *J. Nanopart. Res.* **2010**, *12*, 2125–2133. [[CrossRef](#)]
9. Richter, H.; Howard, J.B. Formation of polycyclic aromatic hydrocarbons and their growth to soot—A review of chemical reaction pathways. *Prog. Energy Combust. Sci.* **2000**, *26*, 565–608. [[CrossRef](#)]
10. Frenklach, M. Reaction mechanism of soot formation in flames. *Phys. Chem. Chem. Phys.* **2002**, *4*, 2028–2037. [[CrossRef](#)]
11. Haynes, B.S.; Wagner, H.G. Soot formation. *Prog. Energy Combust. Sci.* **1981**, *7*, 229–273. [[CrossRef](#)]
12. Wang, H. Formation of nascent soot and other condensed-phase materials in flames. *Proc. Combust. Inst.* **2011**, *33*, 41–67. [[CrossRef](#)]
13. Frenklach, M.; Wang, H. Detailed modeling of soot particle nucleation and growth. *Symp. (Int.) Combust.* **1991**, *23*, 1559–1566. [[CrossRef](#)]
14. D’Anna, A. Combustion-formed nanoparticles. *Proc. Combust. Inst.* **2009**, *32*, 593–613. [[CrossRef](#)]
15. Dobbins, R.A. Hydrocarbon Nanoparticles Formed in Flames and Diesel Engines. *Aerosol Sci. Technol.* **2007**, *41*, 485–496. [[CrossRef](#)]
16. D’Anna, A.; Rolando, A.; Allouis, C.; Minutolo, P.; D’Alessio, A. Nano-organic carbon and soot particle measurements in a laminar ethylene diffusion flame. *Proc. Combust. Inst.* **2005**, *30*, 1449–1456. [[CrossRef](#)]
17. Bartok, W.; Sarofim, A.F. *Fossil Fuel Combustion: A Source Book*; Wiley: New York, NY, USA, 1991.
18. Zhang, Y.; Liu, F.; Lou, C. Experimental and Numerical Investigations of Soot Formation in Laminar Coflow Ethylene Flames Burning in O₂/N₂ and O₂/CO₂ Atmospheres at Different O₂ Mole Fractions. *Energy Fuels* **2018**, *32*, 6252–6263. [[CrossRef](#)]
19. Jain, A.; Das, D.D.; McEnally, C.S.; Pfefferle, L.D.; Xuan, Y. Experimental and numerical study of variable oxygen index effects on soot yield and distribution in laminar co-flow diffusion flames. *Proc. Combust. Inst.* **2019**, *37*, 859–867. [[CrossRef](#)]

20. Cortés, D.; Morán, J.; Liu, F.; Escudero, F.; Consalvi, J.L.; Fuentes, A. Effect of Fuels and Oxygen Indices on the Morphology of Soot Generated in Laminar Coflow Diffusion Flames. *Energy Fuels* **2018**, *32*, 11802–11813. [\[CrossRef\]](#)
21. Escudero, F.; Fuentes, A.; Consalvi, J.L.; Liu, F.; Demarco, R. Unified behavior of soot production and radiative heat transfer in ethylene, propane and butane axisymmetric laminar diffusion flames at different oxygen indices. *Fuel* **2016**, *183*, 668–679. [\[CrossRef\]](#)
22. Wang, Q.; Legros, G.; Bonnet, J.; Morin, C.; Matynia, A.; Consalvi, J.-L.; Liu, F. Experimental assessment of the sudden-reversal of the oxygen dilution effect on soot production in coflow ethylene flames. *Combust. Flame* **2017**, *183*, 242–252. [\[CrossRef\]](#)
23. Shaddix, C.R.; Williams, T.C. The effect of oxygen enrichment on soot formation and thermal radiation in turbulent, non-premixed methane flames. *Proc. Combust. Inst.* **2017**, *36*, 4051–4059. [\[CrossRef\]](#)
24. Contreras, J.; Consalvi, J.L.; Fuentes, A. Oxygen index effect on the structure of a laminar boundary layer diffusion flame in a reduced gravity environment. *Proc. Combust. Inst.* **2017**, *36*, 3237–3245. [\[CrossRef\]](#)
25. Henríquez, R.; Demarco, R.; Consalvi, J.L.; Liu, F.; Fuentes, A. The Oxygen Index on Soot Production in Propane Diffusion Flames. *Combust. Sci. Technol.* **2014**, *186*, 504–517. [\[CrossRef\]](#)
26. Fuentes, A.; Henríquez, R.; Nmira, F.; Liu, F.; Consalvi, J.-L. Experimental and numerical study of the effects of the oxygen index on the radiation characteristics of laminar coflow diffusion flames. *Combust. Flame* **2013**, *160*, 786–795. [\[CrossRef\]](#)
27. Oh, K.C.; Shin, H.D. The effect of oxygen and carbon dioxide concentration on soot formation in non-premixed flames. *Fuel* **2006**, *85*, 615–624. [\[CrossRef\]](#)
28. Kumfer, B.M.; Skeen, S.A.; Chen, R.; Axelbaum, R.L. Measurement and analysis of soot inception limits of oxygen-enriched coflow flames. *Combust. Flame* **2006**, *147*, 233–242. [\[CrossRef\]](#)
29. Lee, K.-O.; Megaridis, C.M.; Zelepouga, S.; Saveliev, A.V.; Kennedy, L.A.; Charon, O.; Ammouri, F. Soot formation effects of oxygen concentration in the oxidizer stream of laminar coannular nonpremixed methane/air flames. *Combust. Flame* **2000**, *121*, 323–333. [\[CrossRef\]](#)
30. Gülder, Ö.L. Effects of oxygen on soot formation in methane, propane, and n-Butane diffusion flames. *Combust. Flame* **1995**, *101*, 302–310. [\[CrossRef\]](#)
31. Wang, L.; Endrud, N.; Turns, S.; D’agostini, M.; Slavejko, A. A study of the influence of oxygen index on soot, radiation, and emission characteristics of turbulent jet flames. *Combust. Sci. Technol.* **2002**, *174*, 45–72. [\[CrossRef\]](#)
32. Merchan-Merchan, W.; McCollam, S.; Pugliese, J.F.C. Soot formation in diffusion oxygen-enhanced biodiesel flames. *Fuel* **2015**, *156*, 129–141. [\[CrossRef\]](#)
33. Beltrame, A.; Porshnev, P.; Merchan-Merchan, W.; Saveliev, A.; Fridman, A.; Kennedy, L.; Petrova, O.; Zhdanok, S.; Amouri, F.; Charon, O. Soot and NO formation in methane–oxygen enriched diffusion flames. *Combust. Flame* **2001**, *124*, 295–310. [\[CrossRef\]](#)
34. Karataş, A.E.; Gülder, Ö.L. Soot formation in high pressure laminar diffusion flames. *Prog. Energy Combust. Sci.* **2012**, *38*, 818–845. [\[CrossRef\]](#)
35. Joo, H.I. Soot Formation in Non-premixed Laminar Flames at Subcritical and Supercritical Pressures. Ph.D. Thesis, University of Toronto, Toronto, ON, Canada, 2010.
36. Bento, D.S.; Thomson, K.A.; Gülder, Ö.L. Soot formation and temperature field structure in laminar propane–air diffusion flames at elevated pressures. *Combust. Flame* **2006**, *145*, 765–778. [\[CrossRef\]](#)
37. Weber, R.; Dugue, J. Combustion Accelerated Swirling Flows in High Confinements. *Prog. Energy Combust. Sci.* **1992**, *18*, 349–367. [\[CrossRef\]](#)
38. Andersson, K.; Johnsson, F. Flame and radiation characteristics of gas-fired O₂/CO₂ combustion. *Fuel* **2007**, *86*, 656–668. [\[CrossRef\]](#)
39. Hjærtstam, S.; Johansson, R.; Andersson, K.; Johnsson, F. Computational Fluid Dynamics Modeling of Oxy-Fuel Flames: The Role of Soot and Gas Radiation. *Energy Fuels* **2012**, *26*, 2786–2797. [\[CrossRef\]](#)
40. Gunnarsson, A.; Simonsson, J.; Bäckström, D.; Mannazhi, M.N.; Bengtsson, P.-E.; Andersson, K. Radiative Heat Transfer Modeling and in Situ Diagnostics of Soot in an 80 kWth Propane Flame with Varying Feed-Gas Oxygen Concentration. *Ind. Eng. Chem. Res.* **2018**, *57*, 12288–12295. [\[CrossRef\]](#)
41. Bäckström, D.; Gunnarsson, A.; Gall, D.; Pei, X.; Johansson, R.; Andersson, K.; Pathak, R.K.; Pettersson, J.B. Measurement of the size distribution, volume fraction and optical properties of soot in an 80 kW propane flame. *Combust. Flame* **2017**, *186*, 325–334. [\[CrossRef\]](#)

42. Simonsson, J.; Gunnarsson, A.; Mannazhi, M.N.; Bäckström, D.; Andersson, K.; Bengtsson, P.E. In-situ soot characterization of propane flames and influence of additives in a 100 kW oxy-fuel furnace using two-dimensional laser-induced incandescence. *Proc. Combust. Inst.* **2019**, *37*, 833–840. [[CrossRef](#)]
43. Richter, H.; Granata, S.; Green, W.H.; Howard, J.B. Detailed modeling of PAH and soot formation in a laminar premixed benzene/oxygen/argon low-pressure flame. *Proc. Combust. Inst.* **2005**, *30*, 1397–1405. [[CrossRef](#)]
44. Fleig, D.; Andersson, K.; Johnsson, F. Influence of operating conditions on SO₃ formation during air and oxy-fuel combustion. *Ind. Eng. Chem. Res.* **2012**, *51*, 9483–9491. [[CrossRef](#)]
45. Allgurén, T.; Andersson, K. Influence of KCl and SO₂ on NO Formation in C₃H₈ Flames. *Energy Fuels* **2017**, *31*, 11413–11423. [[CrossRef](#)]
46. Ekvall, T.; Andersson, K. NO formation and reduction in flames with high feed gas oxygen concentrations. In Proceedings of the Clearwater Clean Energy, Clearwater, FL, USA, 11–15 June 2017.
47. Wang, L.; Haworth, D.C.; Turns, S.R.; Modest, M.F. Interactions among soot, thermal radiation, and NO_x emissions in oxygen-enriched turbulent nonpremixed flames: A computational fluid dynamics modeling study. *Combust. Flame* **2005**, *141*, 170–179. [[CrossRef](#)]



© 2020 by the authors. Licensee MDPI, Basel, Switzerland. This article is an open access article distributed under the terms and conditions of the Creative Commons Attribution (CC BY) license (<http://creativecommons.org/licenses/by/4.0/>).